공학석사 학위논문

Automatic Classification Framework for 3D Positional Relationship between Mandibular Third Molar and Mandibular Canal Using Deep Learning

딥러닝을 이용한 하악 제3대구치와 하악관의 3차원 위치 관계를 위한 자동 분류 프레임워크

2022년 08월

서울대학교 대학원
협동과정 바이오엔지니어링 전공
천 소 영

Automatic Classification Framework for 3D Positional Relationship between Mandibular Third Molar and Mandibular Canal Using Deep Learning

딥러닝을 이용한 하악 제3대구치와 하악관의 3차원 위치 관계를 위한 자동 분류 프레임워크

지도교수 이 원 진

이 논문을 공학석사 학위논문으로 제출함

2022년 08월

서울대학교 대학원

협동과정 바이오엔지니어링 전공

천 소 영

천소영의 공학석사 학위논문을 인준함

2022년 08월

위 원 장 허 민 석 (인)

부 위 원 장 이 원 진 (인)

위 원 허 경 회 (인)

Master Dissertation

Automatic Classification Framework for 3D Positional Relationship between Mandibular Third Molar and Mandibular Canal Using Deep Learning

August 2022

Interdisciplinary Program in Bioengineering
College of Engineering
Seoul National University

So Young Chun

Automatic Classification Framework for 3D Positional Relationship between Mandibular Third Molar and Mandibular Canal Using Deep Learning

Academic advisor **Won Jin Yi**

Submitting a Master Dissertation

August 2022

Interdisciplinary Program in Bioengineering
College of Engineering
Seoul National University

So Young Chun

Confirming the Master Dissertation written by
So Young Chun

August 2022

Chair Heo, Min Suk, D.D.S, Ph.D. (Seal)

Vice Chair Yi, Won Jin, Ph.D. (Seal)

Examiner Huh, Kyung Hoe, Ph.D. (Seal)

Abstract

Automatic Classification Framework for 3D Positional Relationship between Mandibular Third Molar and Mandibular Canal Using Deep Learning

So Young Chun
Interdisciplinary Program in Bioengineering
College of Engineering
Seoul National University

Background: Confirming the relative buccal or lingual relationship with the mandibular canal (MC) is important for appropriate risk assessment and treatment planning for inferior alveolar nerve (IAN) damage during the mandibular third molar extraction. Whereas, for inexperienced clinicians and beginners, identifying the position and path of the mandibular canal in cone-beam computed tomographic (CBCT) images is difficult due to anatomical variation, variable density and noise.

In addition, manual segmentation in each slice of CBCT images is a time-consuming and labor-intensive task. For this reason, this study was performed to develop a computer-aided diagnosis (CAD) framework that can automatically segment both the M3 and the MC on CBCT images and classify the positional relationship between these two structures.

Materials and Methods: The CBCT dataset was divided into a training set (24 patients), validation set (8 patients), and test set (18 patients). At the first stage of the CAD system, an encoder-decoder network was trained to predict the segmentation of both the M3 and the MC in a 2-dimensional (2D) axial slice of CBCT. Then a geometry-guided 3-dimensional (3D) classification network (GCNN) with multiple volume inputs was trained for classifying relative buccal-lingual relationships between the M3 and the MC by learning spatial and geometry information. Afterward, the accuracy of the shape of the mandibular third molar and the mandibular canal and the accuracy of the positional relationship between them predicted through the proposed method were evaluated to whether it was a reasonable CAD system.

Result: In the automatic segmentation, Dense U-Net achieved the dice coefficient similarity values of 0.920±0.131 for the M3 segmentation and DSC values of 0.861±0.096 for the MC segmentation. In the automatic classification of the buccal-lingual relationship between the M3 and the MC, GCNN achieved an accuracy of 1.00.

Conclusion: In this study, a two-step CAD framework was developed to automatically segment both the M3 and the MC on CBCT images and classify the positional relationship between these two structures using deep learning.

Keyword: Deep Learning, Convolutional Neural Network, Segmentation, Classification, Computer-aided diagnosis, Third Molar Extraction Surgery

Student Number: 2020-27763

Table of Contents

List of Tables

List of Figures

List of Abbreviations

CAD	Computer-aided diagnosis
MDCT	Multi-detector computed tomography
CBCT	Cone-beam computed tomography
M3	Mandibular third molar
MC	Mandibular canal
IAN	Inferior alveolar nerve
GCNN	Geometry-guided 3D classification network
CNN	Convolutional Neural Network
DSC	Dice similarity coefficient score
PR	Precision
RC	Recall
RVD	Relative volume difference
VOE	Volume of error
ROC	Receiver operating characteristic
AUC	Area under curve
SDT	Signed distance transform
SDM	Signed distance map
ROI	Region of Interest
VOI	Volume of Interest
FP	False positive
FN	False negative

TP	True positive
TN	True negative
SSM	Statistical shape model
IRB	Institutional review board
ReLU	Rectified linear unit
Grad-CAM	Gradient-weighted Class Activation Mapping

1

Introduction

Mandibular third molar (M3) extraction is one of the most commonly performed surgeries in the oral and maxillofacial field[1-3]. An important complication that can occur in mandibular third molar extraction surgery is nerve damage. In particular, inferior alveolar nerve damage accounts for approximately 0.2 to 8.4%[2]. This attributed to the close positional relationship between the mandibular M3 and the mandibular canal (MC)[4]. As preoperative imaging to predict and minimize complications such as nerve damage, panoramic radiographs have been conventionally used[2, 5, 6]. Since the panoramic radiograph appears on a 2-dimensional (2D) plane, there is a problem with superimposing or distortion of the surrounding anatomical structures. In particular, the positional relationship between the MC and the M3 in the buccal or lingual direction cannot be grasped[4, 7]. To overcome the limitations of such panoramic radiographs, cone-beam computed tomography (CBCT) has been widely used in the dental field[8]. CBCT has the advantage of lower radiation dose and cost compared with multi-detector computed tomography

(MDCT), and clearly shows 3-dimensional (3D) information of anatomical structures including teeth, jaw bone, and neural canal[7, 9, 10].

To predict the relationship between the M3 and the MC from conventional panoramic radiographs, clinicians had to infer specific radiological signs (e.g., darkening or narrowing of the root, bifid apex, interruption or diversion of the cortical outline of the mandibular canal)[11]. On the other hand, the actual buccal or lingual direction can be directly confirmed in the cross-sectional slices of CBCT. In this regard, Maglione et al. classified 6 types according to the distance between the mandibular third molar and the mandibular canal on the CBCT image, the level of contact, and the three-dimensional positional relationship[6]. Wang et al. attempted quantitative classification based on the presence of contact and periradicular, interradicular, buccal, and inferior positions[12].

In addition, Wang et al. analyzed the risk factors for nerve damage on preoperative CBCT images of patients with paresthesia after extraction of the M3[13]. The direct contact relationship between the inferior alveolar neural tube and the root of the M3 and the buccal or lingual position were mentioned as important factors. Moreover, the previous study reported that the possibility of damage to the inferior alveolar nerve is higher if it is located lingually[10]. The rate of the MC passing to the lingual side of the M3 root is high when the MC and the M3 are in contact[14]. Therefore, confirming the relative buccal or lingual relationship with the mandibular canal is important for appropriate risk assessment and treatment planning for inferior alveolar nerve damage during the M3 extraction.

Whereas, for inexperienced clinicians and beginners, identifying the

position and path of the mandibular canal in CBCT images is difficult due to variable density and noise[15]. In addition, manual segmentation in each slice of CBCT images is time-consuming and labor-intensive task. For these reasons, the need for automatic segmentation of mandibular canal in panoramic radiography and CBCT images has emerged.

Previous automatic methods for segmentation include level-set methods[16-20], template-based fitting methods[21], and statistical shape models[22, 23]. There was an issue such as an initialization problem, transformation vulnerability, and additional manual annotation that needed improvement for full automation. Currently, research to segment and classify anatomical structures or lesions using deep learning in medical or dental images has been actively conducted[24], and the performance tends to improve while overcoming limitations depending on the number of data and image modality[25-29]. More recently, studies on various deep learning network models for detecting and segmenting the MCs in CBCT images has been conducted[25, 27].

Liu et al. evaluated the relationship between the M3 and the MC in CBCT images using ResNet-based deep learning method[30]. In their study, the proximity and contact relationship between the M3 and the MC were classified, while the relative buccal or lingual relationship was not included. In this paper, a U-shape network for segmentation of the M3 and the MC and a 3D-convolutional neural network that used geometrical features for the classification of positional relationship between the M3 and the MC were proposed. Therefore, the purpose of this study was to develop a two-stage Computer-aided diagnosis (CAD) framework that performs automatic segmentation of the M3 and the MC on CBCT images and classifies the positional relationship between these two structures using deep learning.

2

Material and Methods

Data acquisition and preparation

The CBCT datasets were collected from patients who underwent dental implant and the M3 extraction surgery at Seoul National University Dental Hospital. All CBCT images were obtained on a CBCT modality (CS 9300, Carestream Health Inc., Rochester, USA) using tube voltage of 80 kVp, a tube current of 8 mA, and had a spatial resolution of 0.2~0.25 mm^3 and size of 841×841 pixels. The CBCT images were collected retrospectively after removing identifiable patient information. This study was performed with approval from the institutional review board of the Seoul National University Dental Hospital (ERI18001). The study was performed in accordance with the Declaration of Helsinki.

The CBCT dataset from patients were divided into a training set (24 patients), validation set (8 patients), and test set (18 patients). A total of 50 patients were split into 24, 8, and 8 patients for training, validation, and test sets, respectively. The number of CBCT axial images was 2735 sections for training set, 811 sections for validation set, and 1801 sections for testing set. In addition, 63 buccal cases and 19 lingual cases were included in the dataset, and the configuration for deep learning classification was shown in the Table 1. Each pixel in all CBCT images was normalized to have a value between 0 and 1 for deep learning input. The M3 and the MC were annotated in CBCT images by an oral and maxillofacial radiologist using a software (3D Slicer, MIT, Cambridge, US)[31] (Fig. 2). The ground truth of annotation for the MC was established by the inferior alveolar nerve surrounded by cortical bone. For buccolingual classification, the positional relationship of the M3 and the MC was defined by analyzing the successive slices from multiplanar images of CBCT. The passing direction and path of the MC were evaluated based on the lamina dura of the M3 root. If the MC directly contacted or passed in close proximity to the inner surface of the M3 root, it was considered a lingual class, and if it directly contacted or passed in close proximity to the outer surface of the M3 root, it was classified as a buccal class (Fig. 1). Cases in which the mandibular canal was located directly below the wisdom tooth were not included.

For segmentation of the M3 and the MC, axial images of CBCT were used to simultaneously segment the M3 and the MC on both sides. Then 3D CBCT volumes cropped per the M3 of the patient were used to classify the positional relationship between the M3 and the MC. In the cases with third molars on both sides, they were flipped to one side (right side) for classification.

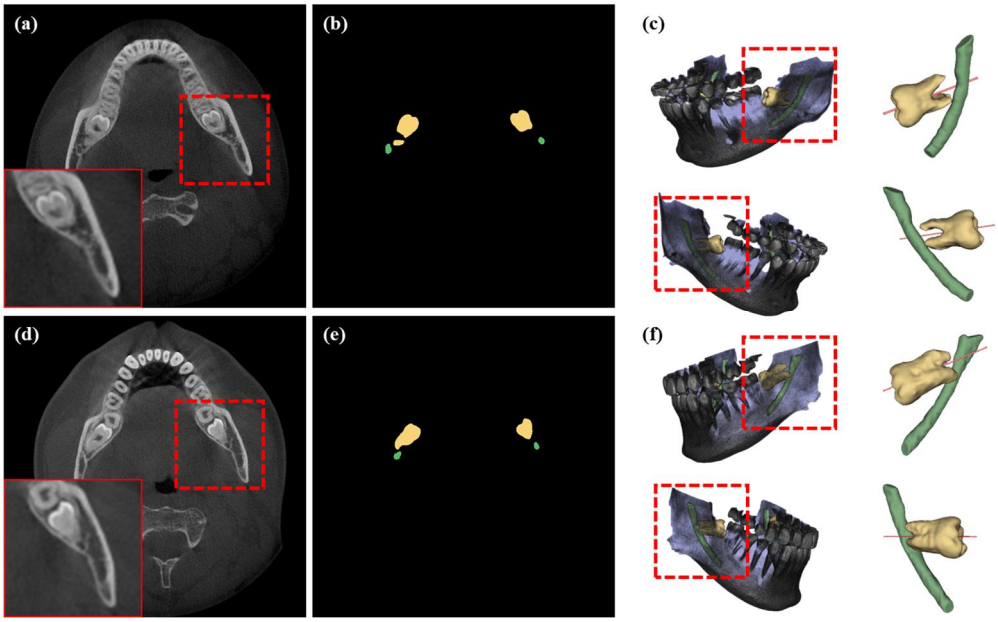

Figure 1. The example of patient who the mandibular canal running the buccal side of the mandibular third molar and the example of patient who the mandibular canal running the lingual side of the mandibular third molar. (a, d) Axial slices of cone beam computed tomography images, (b, e) ground truth of segmentation, and (c, f) 3D visualization of annotated third molars and mandibular canal.

Table 1. The dataset configuration for training deep learning

	Number of patients	Number of axial sections	Number of buccal cases	Number of lingual cases
Train	24	2735	30	6
Validation	8	811	13	2
Test	18	1804	20	11
Total	50	5350	63	19

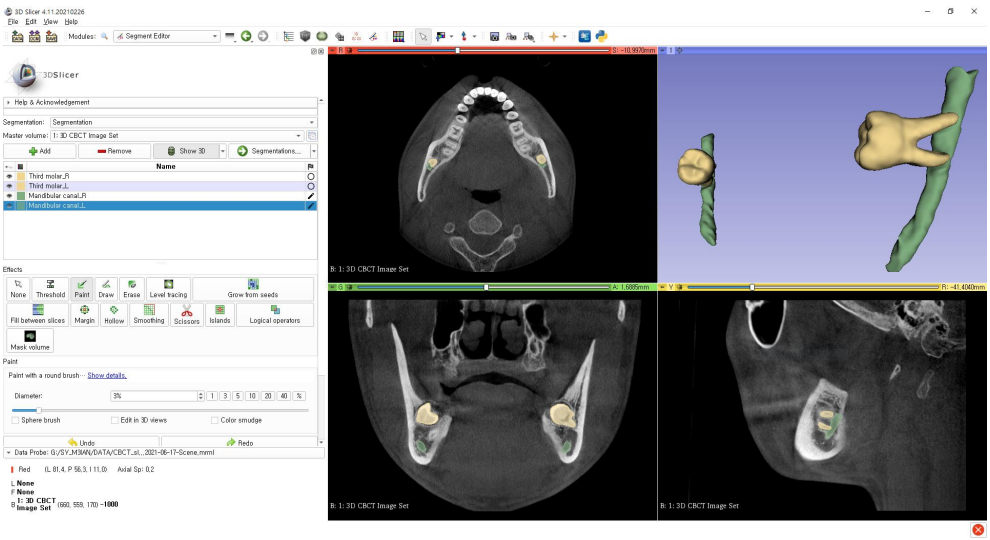

Figure 2. The example visualization of the third molar and the mandibular canal annotated images using 3D slicer software.

Overall architecture of CAD framework for positional relationship between M3 and MC

The proposed method was explicitly explained in this section. Our method consists of segmentation and classification parts as shown in Figure 3. In the segmentation part, an encoder-decoder network was trained to predict the segmentation of both the M3 and the MC in a 2D axial slice of CBCT. In the classification part, a geometry-guided 3D classification network (GCNN) with multiple volume inputs was designed for classifying relative buccal-lingual relationships between the M3 and the MC by learning spatial and geometry information.

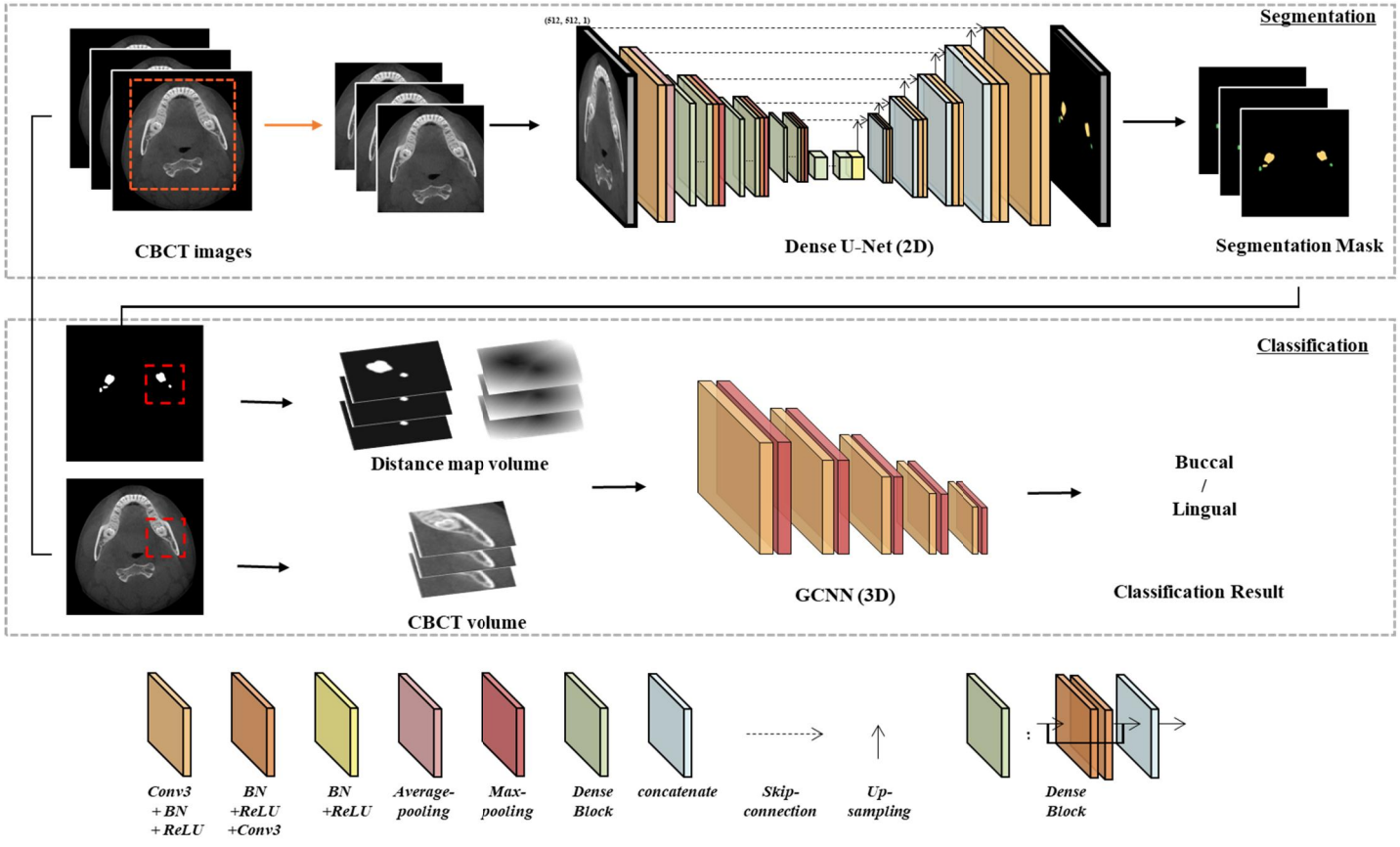

Figure 3. The computer-aided diagnosis framework for classifying the positional relationship between the third molar and the mandibular canal. In the segmentation stage, the third molar and the mandibular canal were simultaneously segmented using Dense U-Net. In the classification stage, the buccal-lingual positional relationship between the third molar and the mandibular canal was classified using the proposed geometry-guided 3D classification network. The geometry-guided 3D classification network included signed distance map with cone beam computed tomography volumes as input and comprised of 3D convolutional neural network.

Segmentation network architecture

CBCT images were automatically cropped into 512x512 pixels images including the region of the mandible. The U-shape network[32-36] has been widely used in medical segmentation tasks and achieved reasonable performance. Inspired by a U-shape network, an encoder-decoder network with a DenseNet121[37] backbone was designed for accurate segmentation of both the M3 and the MC in CBCT images. the DenseNet121 backbone was used as the encoder consisting of multiple densely connected layers and transition layers to improve feature propagation and alleviate vanishing gradients. The decoder part was comprised of a 5-level structure, where each level consisted of a 2×2 up-sampling layer, a skip connection, and two convolutional blocks. The skip connection concatenated up-sampled feature maps with the corresponding those of the encoder path. The convolutional block consisted of a 3×3 convolutional filter, a batch-normalization layer, and rectified linear unit (ReLU) activation function. The *SoftMax* activation function was applied at the last activation layer of the proposed model to extract multi-class segmentation outputs of the M3 and the MC.

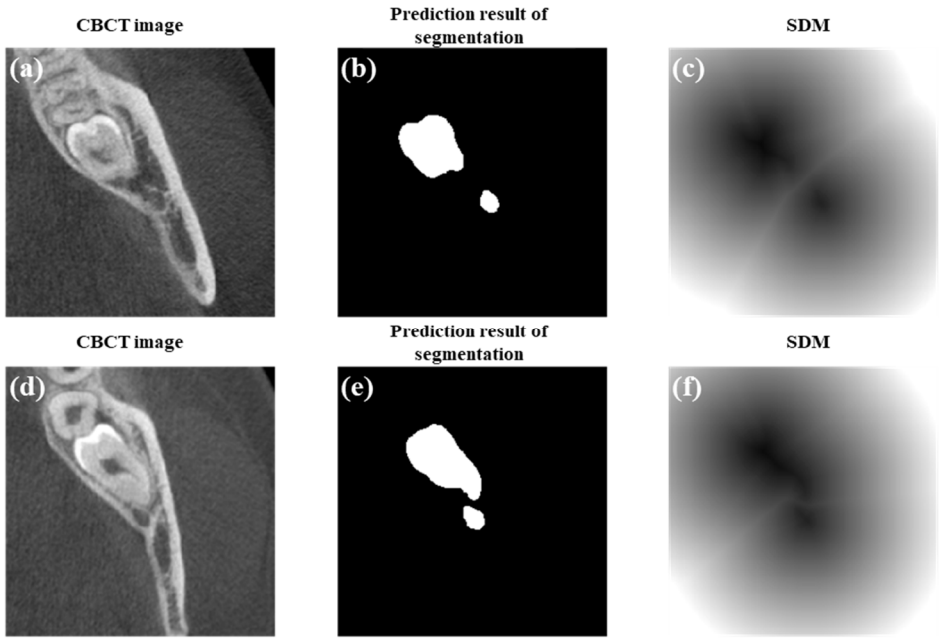

Figure 4. (a-c) The example of patient who the mandibular canal running the buccal side of the mandibular third molar and (d-f) an example of patient who the mandibular canal running the lingual side of the third molar. (a, d) Examples of cone beam computed tomography region of interest at the point closest to the mandibular canal and the third molar, (b, e) segmentation mask of the third molar and the mandibular canal, and (c, f) signed distance map. The line protruding radially was observed in the signed distance map, and the difference in direction was observed when the mandibular canal was passing the lingual side or buccal side**.**

Classification network architecture

For classification, the most important part of the positional relationship determination is the point where the M3 and the MC are in contact or closest to each other. Volume-of-interest (VOI) was extracted with a size of 256x256x32 centered on the point where the M3 and the MC are nearest (Fig. 5). Performing deep learning training in small volumes is efficient because of its lower computing cost, allowing it to be trained rapidly and with few resources.

For relationship classification, the GCNN that simultaneously learns 3D spatial and geometric information using multi-channel inputs was proposed. Our proposed network was composed of two main parts. The first was multiple volume inputs for learning 3D spatial and geometric information. Signed distance transform (SDT)[38] was used to calculate the geometric distance between the M3 and the MC from the segmentation result for the second input to increase the classification accuracy. The SDT, f, was defined as the Euclidean distance from the nearest background point as shown in the following equation $f(x)$:

$$\boldsymbol{f(x)} = \begin{cases} \boldsymbol{d(x, \partial M)} & \boldsymbol{if\ \ x \in M} \\ \boldsymbol{-d(x, \partial M)} & \boldsymbol{if\ \ x \in M^c} \end{cases} \qquad \textbf{Eq. 1}$$

Where x is metric space, M denotes the metric space of the M3 and MC, ∂M denotes the boundary of M[39, 40].

For any $x \in X$,

$$\boldsymbol{d(x, \partial M) := \inf_{y \in \partial M} d(x, y)} \qquad \textbf{Eq. 2}$$

Where inf denotes the infimum.

A signed distance map (SDM) was derived by applying the SDT in 3D as shown in the following equation considering the internal shape of the object and the external relationship.

$$\boldsymbol{SDM} = (\mathbf{1} - \boldsymbol{B}) * \boldsymbol{SDT}(\mathbf{1} - \boldsymbol{B}) - \boldsymbol{B} * (\boldsymbol{SDT}(\boldsymbol{B}) - \mathbf{1}) \quad \textbf{Eq.3}$$

Where B denotes binary segmentation mask of the M3 and the MC, SDT denotes application of the signed distance transform f.

In the SDM, the inside of a boundary of an object was a negative value, and the outside was a positive value. In the SDM of predicted the M3 and the MC result, the values between the boundaries of the two objects form a line that has a constant value. This helps to reveal the spatial relationship between the M3 and the MC, and this can be shown in Fig. 4. In the second, the GCNN with multiple volume inputs was proposed to classify the relative three-dimensional relationship between the M3 and the MC. Our GCNN was comprised of a five-level structure, each level consisted of a 3x3x3 convolutional layer, batch-normalization layer, ReLU activation function, and 2x2x2 max-pooling layer. In the last output part, the class probabilities for the relative buccal-lingual positions of the MC were calculated using the *SoftMax* activation function following the global average pooling layer and dense layer (Fig. 3). Our GCNN simultaneously learned 3D spatial and geometric information from both CBCT volumes and SDM of predicted the M3 and the MC.

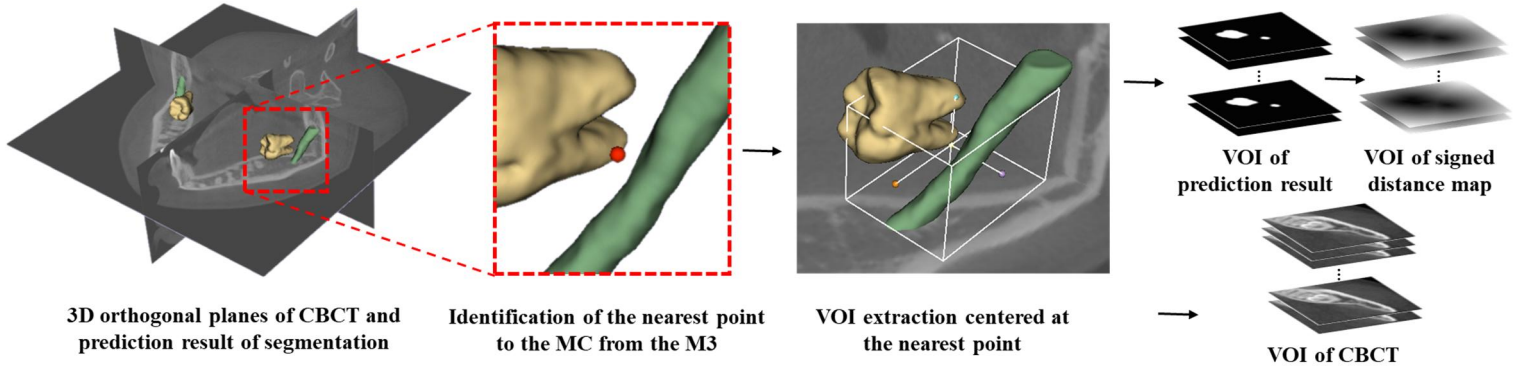

Figure 5. The workflow of extracting volume of interest (VOI) from the stacked cone beam computed tomography and segmentation mask per third molar of the patient. A volume of size 256x256x32 was extracted centered at the nearest point to the mandibular canal (MC) from the third molar (M3).

Evaluation metrics

The performance of segmentation was evaluated by comparing the annotated ground truth with deep learning results of segmentation. The evaluation metrics included volumetric overlap error (VOE), relative volume difference (RVD), precision, recall, dice similarity coefficient (DSC). All matrices were calculated as volume level. VOE $(1 - \frac{V_{gt} \cap V_{pred}}{V_{gt} \cup V_{pred}})$ means a rate between intersection and union, RVD $(\frac{|V_{gt} - V_{pred}|}{V_{gt}})$ means absolute volumetric size difference. Where V_{pred} was the number of voxels from prediction and V_{gt} from annotated ground truth. Precision $(\frac{TP}{TP+FP})$ was a rate of correctly predicted among positive predictions, recall $(\frac{TP}{TP+FN})$ was a rate of correctly predicted among ground truth and DSC $(\frac{2TP}{2TP+FN+FP})$ means a harmonic mean of precision and recall. Where TP, FP, and FN respectively denote true positive, false positive, false negative.

The performance of classification was evaluated using evaluation method as follows: sensitivity, specificity, accuracy and area under receiver operating characteristic curve. Sensitivity $(\frac{TP}{TP+FN})$ was a rate that correctly identifies the positive result for the actual class, specificity $(\frac{TN}{TN+FP})$ was a rate that correctly identifies the negative result for the actual class, and accuracy$(\frac{TP+TN}{TP+TN+FP+FN})$ was the proportion of correct predictions for all classes. Where TN denote true negative.

Interpreting classification result

After training the deep learning network model for classification, the rationality was confirmed by extracting the attentional area of the classification

system. In this study, Grad-CAM was used to verify the target area of buccolingual classification using the GCNN. Grad-CAM verified the learning rationale of the deep learning network model, previously referred to as a black box, by visualizing the learning results of CNN as a heat map. The classification system proposed in this paper utilized the segmentation results and multiple inputs for effective classification. Therefore, a qualitative evaluation was performed by confirming the difference in the attentional area of the classification method according to the segmentation result from each network and the input configuration (Fig. 11) using Grad-CAM.

3

Results

The segmentation performance was evaluated for a total of 18 patient cases not used for training. Table 2 shows the quantitative evaluation of the segmentation performance of DSC, precision, recall, RVD, and VOE. Dense U-Net achieved the highest score for most indicators. Dense U-Net achieved DSC, precision, recall, RVD, and VOE values of 0.920±0.131, 0.946±0.091, 0.918±0.148, 0.039±0.025, and 0.088±0.024, respectively for the M3 segmentation. For the MC segmentation, Dense U-Net achieved DSC, precision, recall, RVD, and VOE of 0.861±0.096, 0.911±0.085, and 0.830±0.136, 0.157±0.0950, 0.248±0.075, respectively.

Table 2. Mean (SD) Dice similarity coefficient score (DSC), precision (PR), recall (RC), relative volume difference (RVD), and volume of error (VOE) by Dense U-Net, Attention U-Net, simple U-Net, and SegNet

M3					
Segmentation Model	DSC	Precision	Recall	RVD	VOE
SegNet	0.898±0.156	0.939±0.093	0.888±0.176	0.049±0.031	0.111±0.027
Simple U-Net	0.902±0.147	0.944±0.092	0.889±0.177	0.056±0.034	0.105±0.034
Attention U-Net	0.916±0.125	0.940±0.086	0.911±0.151	**0.038±0.021**	0.093±0.027
Dense U-Net	**0.920±0.131**	**0.946±0.091**	**0.918±0.148**	0.038±0.025	**0.088±0.024**
MC					
Segmentation Model	DSC	Precision	Recall	RVD	VOE
SegNet	0.770±0.194	0.837±0.171	0.741±0.226	0.162±0.104	0.357±0.146
Simple U-Net	0.825±0.133	0.899±0.106	0.785±0.176	0.192±0.106	0.303±0.114
Attention U-Net	**0.863±0.102**	0.898±0.093	**0.846±0.143**	**0.131±0.074**	0.249±0.077
Dense U-Net	0.861±0.096	**0.911±0.085**	0.830±0.136	0.135±0.071	**0.248±0.075**

Figure 6 shows some qualitative segmentation results of both the M3 and the MC in CBCT axial images. The predicted segmentation masks of M3&MC (red) from the segmentation networks and the ground-truth of M3&MC (green) were overlaid on the original CBCT images. In Figure 6 (a), (d), and (e), the segmentation result from Dense U-Net has more true positives and fewer false negatives in the MC area. Particularly, in Figure 6(a), the MC was difficult to identify visually. In contrast to other segmentation networks that failed to successfully segment the MC, Dense U-Net successfully segmented the MC. In addition, the segmentation result of Dense U-Net has fewer false positives compared with the segmentation result of other networks as in Figure 6 (c).

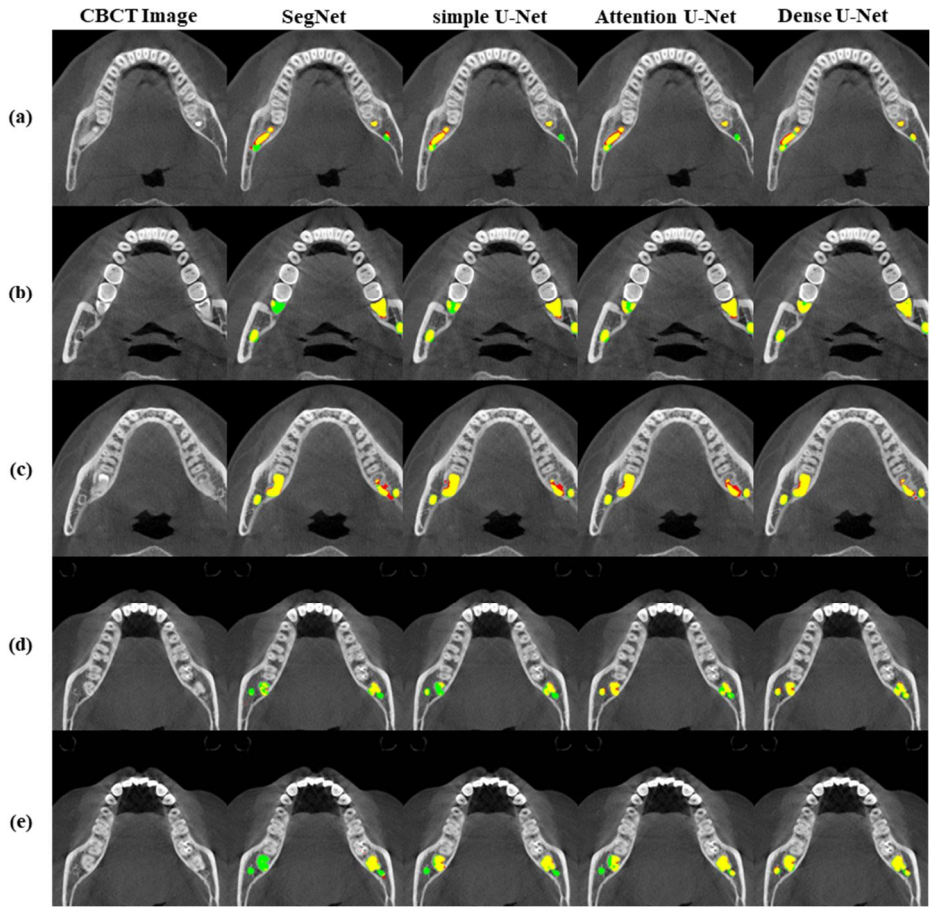

Figure 6. Segmentation results from SegNet, Simple U-Net, Attention U-Net, and Dense U-Net. The predicted segmentation masks of the third molar and the mandibular canal and the ground-truth of those were overlaid on the original cone beam computed tomography images. The green, yellow, and red regions represent the false negative, the true positive, and the false positive, respectively.

Figure 7 shows the 3D visualizations of 2D segmentation results from each network. The 3D visual results of Dense U-Net show in general agreement with the ground truth without frequent discontinuities compared with other networks, indicating a lower level of false negative than those of the other networks. Figure 8 shows the precision-recall curves representing the segmentation performance of SegNet, simple U-Net, Attention U-Net, and Dense U-Net for the M3 (a), the MC (b), the M3 and the MC (c). Dense U-Net achieved (a) 0.9571, (b) 0.8717, and (c) 0.9363 in the area under curve values of the precision-recall curve for the M3, the MC, the M3 with the MC, respectively. These were the highest values compared with the AUCs from other networks. Figure 9 shows the line plots of DSC, precision, and recall of the M3 and the MC. Computed values were averaged mean DSC of a same axial slice from deep networks from the inferior to the superior part of the CBCT volumes and plotted for each deep learning network. The results of Dense U-Net had higher values and more minor fluctuations in the lines plot than other results.

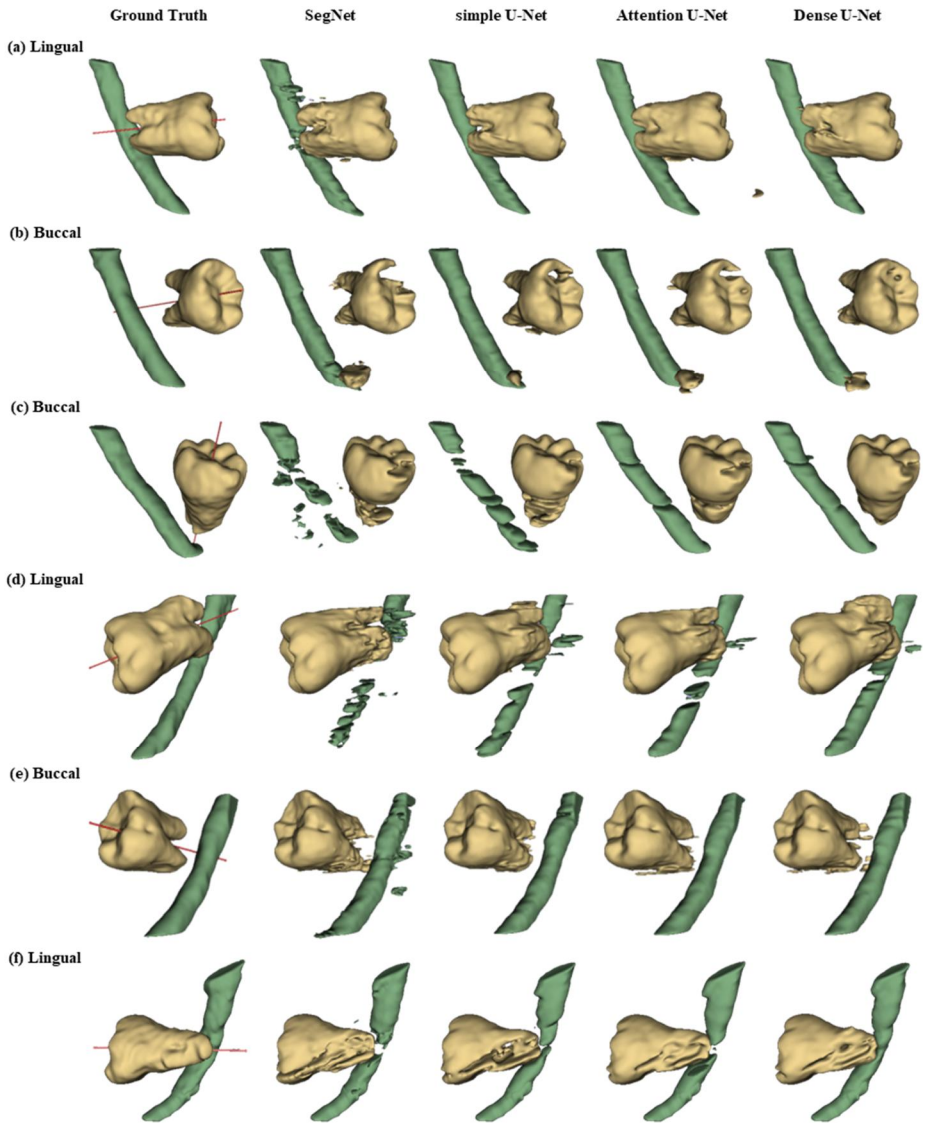

Figure 7. Three-dimensional visualization of ground truth, Three-dimensional visualization of segmentation results from SegNet, Simple U-Net, Attention U-Net, and Dense-U-Net from right to left. (a-c) Third molars and mandibular canals at the right side of patients, (d-f) third molars and mandibular canals at the left side of patients. The red line passing through each third molar was the main axis of the third molar, traversing the center of the root of the tooth from the center of the tooth crown. The direction of the red line explicitly confirmed the buccal-lingual relationship between the third molar and the mandibular canal.

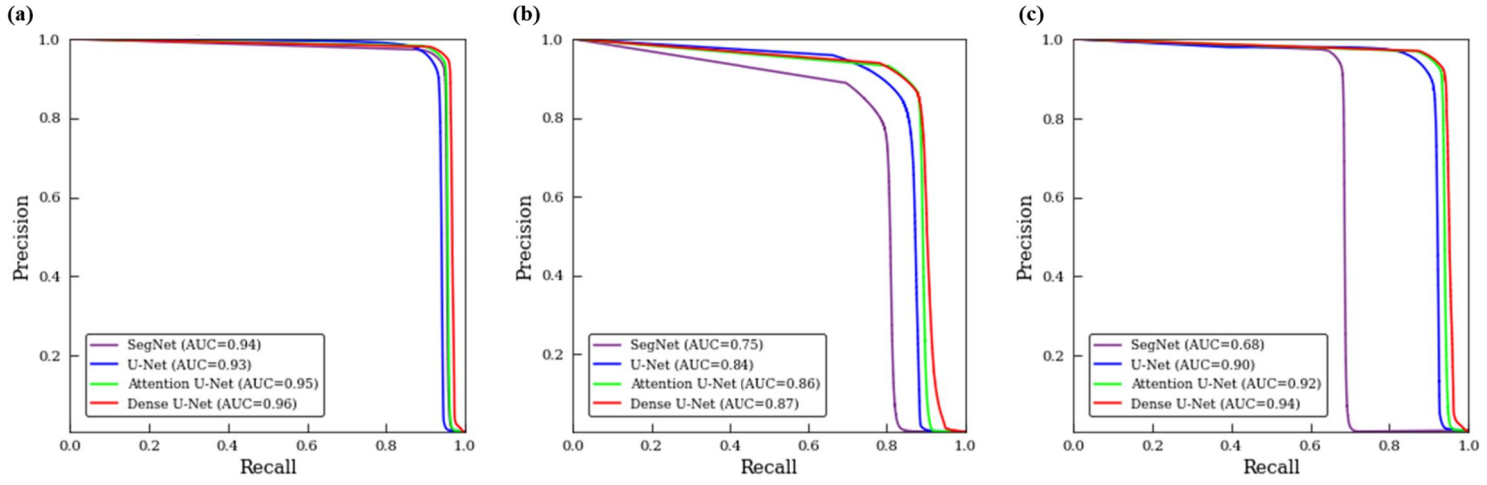

Figure 8. Precision-recall curves from segmentation results of (a) the third molar, (b) the mandibular canal, and (c) the third molar with the mandibular canal**.**

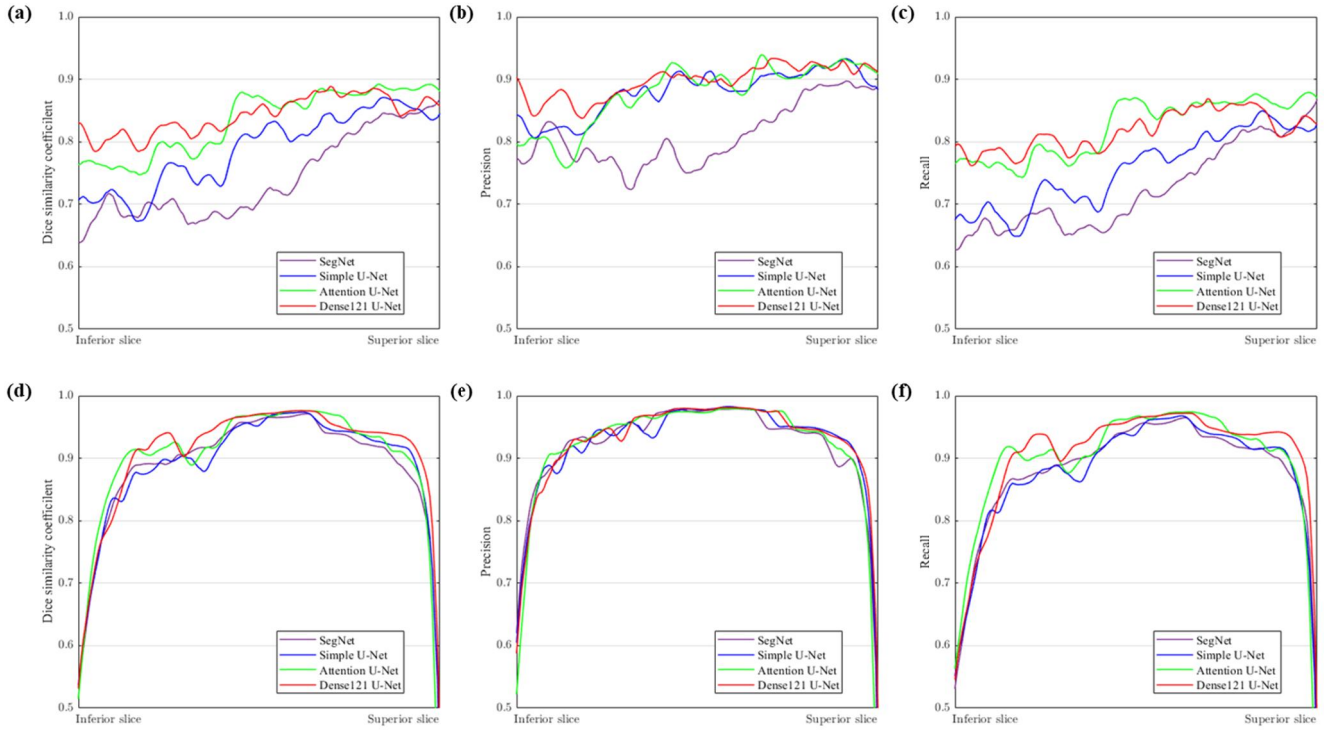

Figure 9. The line plots of dice similarity coefficient, precision, recall from Dense U-Net, Attention U-Net, simple U-Net, and SegNet. Each metric was calculated in an axial slice from the inferior to the superior aspect of the cone beam computed tomography. (a-c) The results of the third molar segmentation, (d-f) the results of the mandibular canal segmentation.

Table 3 shows the quantitative results of a comparative experiment on classification performance to prove the validity of the input components of the GCNN consisting of multi-channel input, including the SDM. The result of training the three-dimensional positional relationship with only the CBCT volume showed the lowest accuracy, sensitivity, and AUC, indicating the classification failed. In addition, most of the results of the different input combinations were highly imbalanced. On the other hand, the highest values were achieved with accuracy, sensitivity, specificity, and area under the ROC curve where the Dense U-Net segmentation results were utilized for SDM generation, which was employed as the second channel of multi-input. Figure 10 shows the ROC curve for verifying the performance of the GCNN. The classification performance using the segmentation result of Dense U-Net is closest to the upper left, indicating the best classifier.

The segmentation performance affected the classification performance because the SDM, a component of the GCNN, was derived from the result of the segmentation. Binary masks provided location information and shape information in the training of classification even though discontinuities of segmentation results frequently appeared. This can be explained that a coherent region was emphasized as a target for classification training in Fig. 12. In contrast to a binary mask representing a distinct region, even if successive segmentation of the M3 and the MC fails, the SDM displayed a fine linear structure. In the case of the SDM derived from segmentation results with poor accuracy and discontinuity, fragmented and scattered white linear structures were shown, resulting in images that were difficult to represent proper relationships between the M3 and the MC. Accordingly, reduced classification performance was shown when using SDM of SegNet and Simple Unet,

which have relatively low segmentation performance, and significantly increased classification performance when the SDM of Attention U-Net and Dense U-Net was used. The training of classification using only the SDM as input still does not seem to target reasonable regions well. On the other hand, as suggested in this paper, if the SDM was used with CBCT volume for the classification training, training targeted a reasonable area with high consistency. Our assumption that the additional information on the regions closest to the M3 and the MC and the position and shape of adjacent anatomical structures would be an important basis for classification training was verified.

Fig. 12 shows some representative cases of applying Grad-CAM to classification results. The activation heatmaps of Grad-CAM overlaying on the patient's CBCT images were shown, according to the segmentation network and the input configuration of the classification network.

Table 3. Comparative analysis of the geometry-guided 3-dimensional classification network for classification performance. Accuracy, sensitivity, specificity, and area under the receiver operating characteristic (ROC) curve (AUC) values for classification performance of the buccal-lingual relationship between the third molar and the mandibular canal.

Segmentation model	CBCT	Binary mask	Distance map	Accuracy	Sensitivity	Specificity	AUC of ROC
-	√			0.32	0.10	0.73	0.34
SegNet		√		0.87	0.90	0.82	0.97
Simple U-Net		√		0.74	1.00	0.27	1.00
Attention U-Net		√		0.61	0.50	0.82	0.81
Dense U-Net		√		0.84	1.00	0.55	0.91
SegNet	√	√		0.48	0.25	0.91	0.69
Simple U-Net	√	√		0.77	0.80	0.73	0.83
Attention U-Net	√	√		0.52	0.40	0.73	0.62
Dense U-Net	√	√		0.71	1.00	0.18	0.69
SegNet			√	0.77	0.65	1.00	0.91
Simple U-Net			√	0.84	0.80	0.91	0.96
Attention U-Net			√	0.71	0.85	0.45	0.85
Dense U-Net			√	0.84	0.90	0.73	0.92
SegNet	√		√	0.65	0.65	0.64	0.76
Simple U-Net	√		√	0.68	1.00	0.09	0.92
Attention U-Net	√		√	0.90	0.90	0.91	0.98
Dense U-Net	√		√	**1.00**	**1.00**	**1.00**	**1.00**

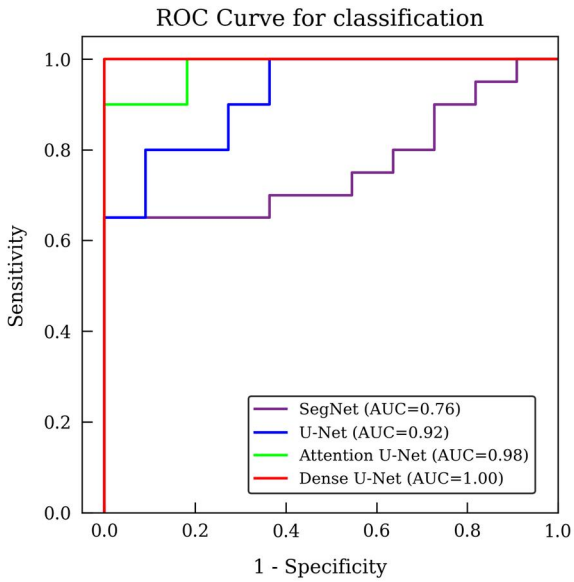

Figure 10. The performance of buccolingual classification in terms of receiver operating characteristic curves. Classification performance using geometry-guided 3D classification network was presented for segmentation networks of SegNet, U-Net, Attention U-Net, and Dense U-Net.

4

Discussion and Conclusion

The detection of the inferior alveolar nerve is a necessary step in oral and maxillofacial surgery, such as implant placement in the mandible, extraction of impacted teeth, and orthognathic surgery[1-3, 41]. If nerve damage occurs during surgery, it may cause temporary or permanent sensory and functional abnormalities, affecting the patients quality of life[42]. The incidence of inferior alveolar nerve injuries in the M3 extraction surgery increases as the MC and the root of the M3 are closely located[43]. In addition, the positional relationship in the buccolingual aspect of the MC to the M3 is a risk factor as important as proximity between the M3 and the MC for nerve damage and a factor that is routinely classified in the clinical field[13, 44]. Therefore, preoperative imaging and diagnosis are essential to sufficiently predict and prepare for the risk. Conventionally used 2D panoramic images have limitations such as distortion and superimposing of structures[4, 7]. The CBCT images, which overcome these problems have been widely used in recent years[8]. However, it is a labor-consuming task to accurately identify the path of the MC and the three-dimensional relationship with the M3, in each cross-section of the CBCT image

which has lower contrast resolution and higher noise[15].

The application of deep learning to diagnosis and prognosis in the medical field as well as in the dental field has been actively conducted. These include segmentation of the M3 or the MC on 2D panoramic radiography or 3D CT or CBCT images[25, 27, 29, 45-48] and classification of impacted third molars[49-52]. In particular, Liu et al. segmented the M3 and MC on CBCT images and classified the positional relationship into three types according to the proximity and contact between the two structures[30]. However, no previous studies have yet been reported on the automatic classification of the buccal-lingual positional relationship between the M3 and the MC using deep learning.

In this study, a two-stage deep learning CAD framework was proposed to automatically segment the M3 and the MC and classify the positional relationship between the M3 and the MC in the CBCT images. In the first stage, a U-shaped architecture was proposed for multi-class segmentation of the M3 and the MC, where the encoder path is built using pre-trained DenseNet121[37]. In the second stage, the GCNN learns anatomical geometric information in the CBCT volumes using a signed distance map (SDM)[38] generated from a segmentation mask of the M3 and the MC to accurately classify their positional relationship.

Before classifying the positional relationship between the M3 and the MC, the M3 and the MC were segmented using Dense U-Net, the deep learning model that effectively reused features of objects. In the case of the M3 segmentation, all four network models showed high segmentation performance, but Dense U-Net showed the highest segmentation result. In the case of the MC segmentation,

Attention U-Net and Dense U-Net showed higher results than the other two networks (Table 2). In the AUC values of the precision-recall curve, Dense U-Net had the highest value in all segmentation results, indicating that the Dense- Dense U-Net was a network with balanced precision and recall. (Fig. 8). In the result of superimposing the predicted mask and the ground truth for qualitative evaluation, fewer false-positive (red color) and false negative (green color) areas were observed in the result of Dense U-Net compared with the results of the other networks (Fig. 6). When the segmentation result was visualized in performance, disconnectivity of the MC occurred in the region where the border of the cortex of the MC was not clearly observed on the CBCT image, or where the MC was compressed or interrupted by the root of the M3. Conversely, discontinuous points were significantly reduced in the results of Dense U-Net (Figs. 6, 7, and 9). This was demonstrated numerically by finding higher values and more minor fluctuations in the lines plotting the results of the Dense U-Net (Fig. 9). As shown in Figures 6-8, the Dense U-Net was an effective network for seamlessly segmenting all target objects.

To classify the relative positional relationship between the M3 and the MC, the GCNN was designed utilizing the SDM that provided additional three-dimensional spatial information. A comparative study was performed to validate the effect of the SDM used as multiple volume inputs together with CBCT, which was the component of the GCNN. The result of classification using the proposed GCNN was the highest with 1.00 AUC (Table 3, Fig. 10). In this case, the SDM of the proposed GCNN was generated as a result of Dense U-Net. the GCNN trained using both 3D CBCT volumes and the SDM as multi-channel inputs showed higher performance than other combinations of inputs. In particular, the classification

accuracy using the SDM, which transformed results of Attention U-Net or Dense U-Net, was 0.9 or higher, which was higher than the results of other networks used. On the other hand, when single-channel inputs were used, the sensitivity or specificity values were significantly lower. In addition, adding CBCT volume as a multi-channel input resulted in lower accuracy. These results show that there is a limitation to extracting 3D position information from a binary mask. It also demonstrates that the complexity of the positional relationship analysis increases when the CBCT volume is applied as a multi-channel input.

The quantitively confirmed classification performance was qualitatively interpreted by Grad-CAM, confirming the target area for buccal-lingual classification of the GCNN (Fig. 12). The most reasonable Grad-CAM was observed when using our suggested GCNN, CBCT with the distance map produced by the segmentation result of Dense U-Net as an input of classification. Unlike other methods that targeted the entire M3, mandible, or external regions unrelated to classification, the proposed method targeted the root of the M3 and periphery of the MC. In the case of the lingual class predicted with the GCNN, the shape of the M3 root and the medullary space, including or adjacent to the cortical layer of the MC, was recognized. In most cases of the buccal class predicted with the GCNN, the marginal area of the M3 and the medullary space adjacent to the cortical layer of the MC were recognized. Grad-CAM confirmed that the GCNN predicted buccal-lingual class by an overall consistent region, especially anatomical structures close to the M3 and the MC. In other words, the GCNN served as a geometric guide providing specific location and spatial information of the M3 and the MC in the classification process. As a result, the GCNN model acquired reasonable

classification performance.

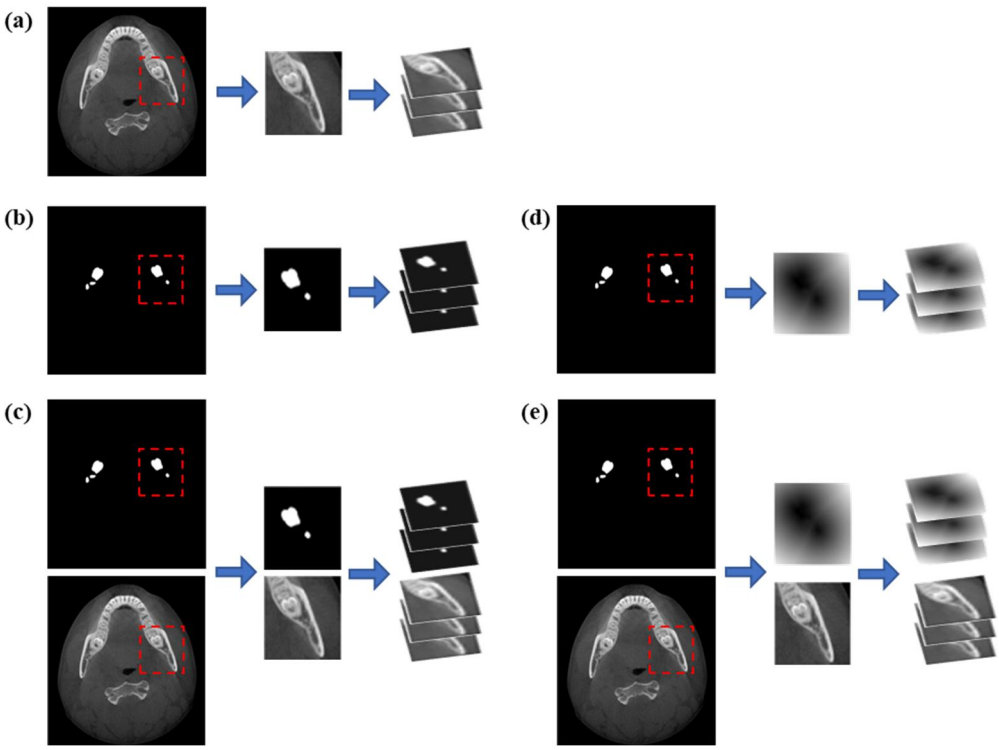

Figure 11. Input configurations for the comparative experiment. (a) Cone beam computed tomography image only, (b) binary mask only, (c) cone beam computed tomography image with the binary mask, (d) The signed distance map only, and (e) cone beam computed tomography image with the signed distance map.

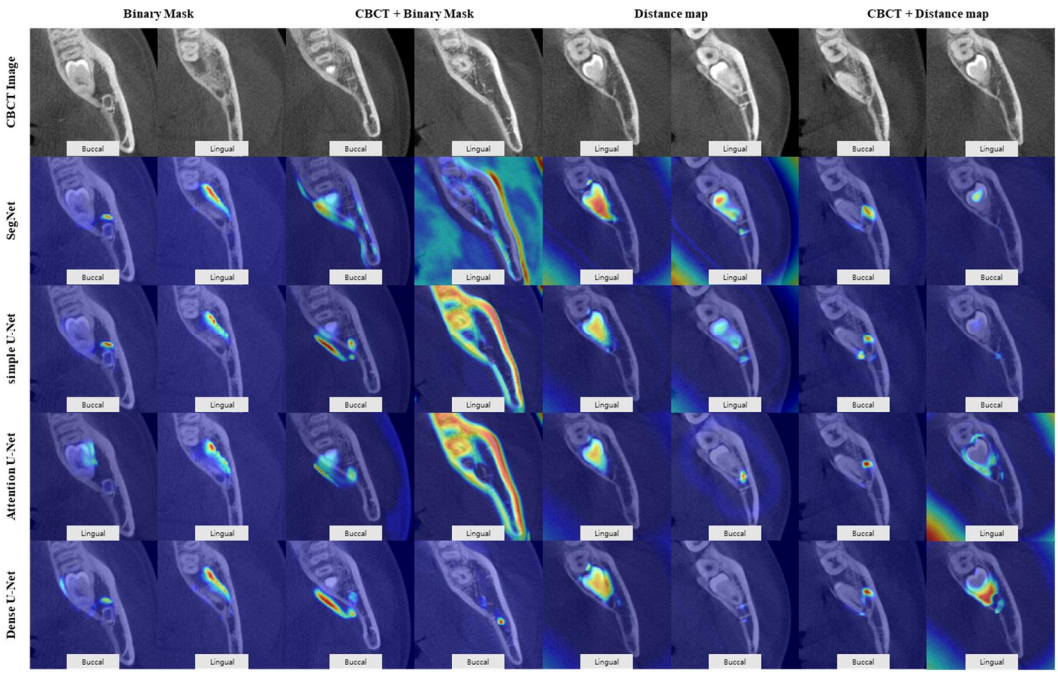

Figure 12. Visualization results of Grad-CAM from SegNet, Simple U-Net, Attention U-Net, and Dense U-Net. Grad-CAM result when the input image configuration was (a) binary mask only (b) cone beam computed tomography with binary mask (c) signed distance map only (d) cone beam computed tomography with signed distance map. Ground truth and predicted class name was shown on the bottom of each image.

Our proposed framework automated the classification of the positional relationship between the M3 and the MC, which was often performed in clinical practice. The developed CAD framework performed segmentation of the M3 and the MC in the first stage. In the second stage, spatial information was extracted from the result of segmentation through the SDT, and the buccal-lingual relationship between the M3 and the MC was classified. The segmentation mask sufficient to identify the M3 and the MC was obtained, and DSC values of 0.920±0.131 and 0.0.861±0.096 were achieved, for the M3 and the MC, respectively. Then, the GCNN achieved an accuracy of 1.00 in that automatic classification of the positional relationship between the M3 and the MC, which can help in the preoperative image examination of the M3 extraction operation. This presented more explicit three-dimensional information than simply analyzing CBCT images as a multiplanar. In addition, our deep learning segmentation network served as a guide for CBCT images that were difficult to read since the segmentation mask overlaid on the CBCT image. Moreover, the decision-making time of clinicians could be shortened by receiving a kind of proposal for cross-checking through the automatic classification of buccal relation, which is the goal of this framework.

In our method, the segmentation step must precede the classification step. The classification performance depended on the segmentation performance, but the training process did not affect each other. Therefore, a new framework combining the segmentation and the classification, two training losses with adjustable weights, would be discussed in future studies. For lack of data, only buccal and lingual position was used as the criterion for classification in this study. The M3 appears in various positions and orientations, and the MC can travel between or below the roots

of the M3. In future research, an in-depth discussion on the diversification of classification and criteria for ambiguous cases should be made. In this study, the annotation process for the supervised training of segmentation was semi-automated using a 3D slicer; nevertheless, labeling the M3 and MC for each slice is still time and labor-consuming. There is a necessity to improve the efficiency of annotation processing on the acquired training data. Another limitation is that CBCT images of similar quality with the same equipment were used. For future studies, evaluating performance of the network on various CBCT images with different imaging equipment or scanning conditions is regarded.

In conclusion, a deep-learning CAD framework was proposed for the M3 extraction surgery, including the segmentation of the M3 and the MC and the classification of positional relationships between them. This approach was an outstanding tool for automating preoperative tasks such as classifying positional relationships in the M3 extraction surgery and identifying the shape of the M3 and MC in three dimensions through 3D visualization of the segmentation result.

5

References

1. Sayed N, Bakathir A, Pasha M, Al-Sudairy S. Complications of third molar extraction: a retrospective study from a tertiary healthcare centre in Oman. Sultan Qaboos University Medical Journal 2019;19e230.

2. Leung Y, Cheung L. Risk factors of neurosensory deficits in lower third molar surgery: a literature review of prospective studies. International Journal of Oral and Maxillofacial Surgery 2011;40:1-10.

3. Bui CH, Seldin EB, Dodson TB. Types, frequencies, and risk factors for complications after third molar extraction. Journal of Oral and Maxillofacial Surgery. 2003;61:1379-89.

4. Hasegawa T, Ri S, Shigeta T, Akashi M, Imai Y, Kakei Y, et al. Risk factors associated with inferior alveolar nerve injury after extraction of the mandibular third molar—a comparative study of preoperative images by panoramic radiography and computed tomography. International Journal of Oral and Maxillofacial Surgery 2013;42:843-51.

5. Jerjes W, Upile T, Shah P, Nhembe F, Gudka D, Kafas P, et al. Risk factors

associated with injury to the inferior alveolar and lingual nerves following third molar surgery—revisited. Oral Surgery Oral Medicine Oral Pathology Oral Radiology and Endodontology 2010;109:335-45.

6. Maglione M, Costantinides F, Bazzocchi G. Classification of impacted mandibular third molars on cone-beam CT images. Journal of Clinical and Experimental Dentistry 2015;7:e224.

7. Maegawa H, Sano K, Kitagawa Y, Ogasawara T, Miyauchi K, Sekine J, et al. Preoperative assessment of the relationship between the mandibular third molar and the mandibular canal by axial computed tomography with coronal and sagittal reconstruction. Oral Surgery Oral Medicine Oral Pathology Oral Radiology and Endodontology. 2003;96:639-46.

8. Matzen L, Wenzel A. Efficacy of CBCT for assessment of impacted mandibular third molars: a review–based on a hierarchical model of evidence. Dentomaxillofacial Radiology. 2015;44:20140189.

9. Ueda M, Nakamori K, Shiratori K, Igarashi T, Sasaki T, Anbo N, et al. Clinical significance of computed tomographic assessment and anatomic features of the inferior alveolar canal as risk factors for injury of the inferior alveolar nerve at third molar surgery. Journal of Oral and Maxillofacial Surgery. 2012;70:514-20.

10. Ghaeminia H, Meijer G, Soehardi A, Borstlap W, Mulder J, Bergé S. Position of the impacted third molar in relation to the mandibular canal. Diagnostic accuracy of cone beam computed tomography compared with panoramic radiography. International Journal of Oral and Maxillofacial Surgery. 2009;38:964-71.

11. Blaeser BF, August MA, Donoff RB, Kaban LB, Dodson TB. Panoramic

radiographic risk factors for inferior alveolar nerve injury after third molar extraction. Journal of Oral and Maxillofacial Surgery. 2003;61:417-21.

12. Wang W-Q, Chen MY, Huang H-L, Fuh L-J, Tsai M-T, Hsu J-T. New quantitative classification of the anatomical relationship between impacted third molars and the inferior alveolar nerve. BMC Medical Imaging. 2015;15:1-6.

13. Wang D, Lin T, Wang Y, Sun C, Yang L, Jiang H, et al. Radiographic features of anatomic relationship between impacted third molar and inferior alveolar canal on coronal CBCT images: risk factors for nerve injury after tooth extraction. Archives of Medical Science: AMS. 2018;14:532.

14. Gu L, Zhu C, Chen K, Liu X, Tang Z. Anatomic study of the position of the mandibular canal and corresponding mandibular third molar on cone-beam computed tomography images. Surgical and Radiologic Anatomy. 2018;40:609-14.

15. Pauwels R, Jacobs R, Singer SR, Mupparapu M. CBCT-based bone quality assessment: are Hounsfield units applicable? Dentomaxillofacial Radiology. 2015;44:20140238.

16. Gan Y, Xia Z, Xiong J, Li G, Zhao Q. Tooth and alveolar bone segmentation from dental computed tomography images. IEEE Journal of Biomedical and Health Informatics. 2017;22:196-204.

17. Hosntalab M, Aghaeizadeh Zoroofi R, Abbaspour Tehrani-Fard A, Shirani G. Segmentation of teeth in CT volumetric dataset by panoramic projection and variational level set. International Journal of Computer Assisted Radiology and Surgery. 2008;3:257-65.

18. Gao H, Chae O. Individual tooth segmentation from CT images using level set method with shape and intensity prior. Pattern Recognition. 2010;43:2406-17.

19. Ji DX, Ong SH, Foong KWC. A level-set based approach for anterior teeth segmentation in cone beam computed tomography images. Computers in Biology and Medicine. 2014;50:116-28.

20. Moris B, Claesen L, Sun Y, Politis C, editors. Automated tracking of the mandibular canal in cbct images using matching and multiple hypotheses methods. 2012 Fourth International Conference on Communications and Electronics (ICCE); 2012: IEEE.

21. Barone S, Paoli A, Razionale AV. CT segmentation of dental shapes by anatomy-driven reformation imaging and B-spline modelling. International Journal for Numerical Methods in Biomedical Engineering. 2016;32:e02747.

22. Abdolali F, Zoroofi RA, Abdolali M, Yokota F, Otake Y, Sato Y. Automatic segmentation of mandibular canal in cone beam CT images using conditional statistical shape model and fast marching. International Journal of Computer Assisted Radiology and Surgery. 2017;12:581-93.

23. Kainmueller D, Lamecker H, Seim H, Zinser M, Zachow S, editors. Automatic extraction of mandibular nerve and bone from cone-beam CT data. International Conference on Medical Image Computing and Computer-Assisted Intervention; 2009: Springer.

24. Hwang J-J, Jung Y-H, Cho B-H, Heo M-S. An overview of deep learning in the field of dentistry. Imaging Science in Dentistry. 2019;49:1-7.

25. Kwak GH, Kwak E-J, Song JM, Park HR, Jung Y-H, Cho B-H, et al. Automatic mandibular canal detection using a deep convolutional neural network. Scientific Reports. 2020;10:1-8.

26. Cui Z, Li C, Wang W, editors. ToothNet: automatic tooth instance

segmentation and identification from cone beam CT images. Proceedings of the IEEE/CVF Conference on Computer Vision and Pattern Recognition; 2019.

27. Jaskari J, Sahlsten J, Järnstedt J, Mehtonen H, Karhu K, Sundqvist O, et al. Deep learning method for mandibular canal segmentation in dental cone beam computed tomography volumes. Scientific Reports. 2020;10:1-8.

28. Litjens G, Kooi T, Bejnordi BE, Setio AAA, Ciompi F, Ghafoorian M, et al. A survey on deep learning in medical image analysis. Medical Image Analysis. 2017;42:60-88.

29. Vinayahalingam S, Xi T, Bergé S, Maal T, de Jong G. Automated detection of third molars and mandibular nerve by deep learning. Scientific Reports. 2019;9:1-7.

30. Liu M-Q, Xu Z-N, Mao W-Y, Li Y, Zhang X-H, Bai H-L, et al. Deep learning-based evaluation of the relationship between mandibular third molar and mandibular canal on CBCT. Clinical Oral Investigations. 2022;26:981-91.

31. Fedorov A, Beichel R, Kalpathy-Cramer J, Finet J, Fillion-Robin J-C, Pujol S, et al. 3D Slicer as an image computing platform for the Quantitative Imaging Network. Magnetic Resonance Imaging. 2012;30:1323-41.

32. Ronneberger O, Fischer P, Brox T, editors. U-net: Convolutional networks for biomedical image segmentation. International Conference on Medical Image Computing and Computer-assisted Intervention; 2015: Springer.

33. Zhou Z, Rahman Siddiquee MM, Tajbakhsh N, Liang J. Unet++: A nested u-net architecture for medical image segmentation. Deep learning in medical image analysis and multimodal learning for clinical decision support: Springer; 2018. p. 3-11.

34. Milletari F, Navab N, Ahmadi S-A, editors. V-net: Fully convolutional neural networks for volumetric medical image segmentation. 2016 Fourth International Conference on 3D Vision (3DV); 2016: IEEE.

35. Alom MZ, Hasan M, Yakopcic C, Taha TM, Asari VK. Recurrent residual convolutional neural network based on u-net (r2u-net) for medical image segmentation. arXiv preprint arXiv:180206955. 2018.

36. Oktay O, Schlemper J, Folgoc LL, Lee M, Heinrich M, Misawa K, et al. Attention u-net: Learning where to look for the pancreas. arXiv preprint arXiv:180403999. 2018.

37. Huang G, Liu Z, Van Der Maaten L, Weinberger KQ, editors. Densely connected convolutional networks. Proceedings of the IEEE Conference on Computer Vision and Pattern Recognition; 2017.

38. Ye Q-Z, editor The signed Euclidean distance transform and its applications. 9th International Conference on Pattern Recognition; 1988: IEEE Computer Society.

39. Malladi R, Sethian JA, Vemuri BC. Shape modeling with front propagation: A level set approach. IEEE Transactions on Pattern Analysis and Machine Intelligence. 1995;17:158-75.

40. Chan T, Zhu W, editors. Level set based shape prior segmentation. 2005 IEEE Computer Society Conference on Computer Vision and Pattern Recognition (CVPR'05); 2005: IEEE.

41. Juodzbalys G, Wang HL, Sabalys G, Sidlauskas A, Galindo-Moreno P. Inferior alveolar nerve injury associated with implant surgery. Clinical Oral Implants Research. 2013;24:183-90.

42. Abarca M, van Steenberghe D, Malevez C, De Ridder J, Jacobs R.

Neurosensory disturbances after immediate loading of implants in the anterior mandible: an initial questionnaire approach followed by a psychophysical assessment. Clinical Oral Investigations. 2006;10:269-77.

43. Sarikov R, Juodzbalys G. Inferior alveolar nerve injury after mandibular third molar extraction: a literature review. Journal of Oral & Maxillofacial Research. 2014;5.

44. Tachinami H, Tomihara K, Fujiwara K, Nakamori K, Noguchi M. Combined preoperative measurement of three inferior alveolar canal factors using computed tomography predicts the risk of inferior alveolar nerve injury during lower third molar extraction. International Journal of Oral and Maxillofacial Surgery. 2017;46:1479-83.

45. Dhar MK, Yu Z. Automatic tracing of mandibular canal pathways using deep learning. arXiv preprint arXiv:211115111. 2021.

46. Lahoud P, Diels S, Niclaes L, Van Aelst S, Willems H, Van Gerven A, et al. Development and validation of a novel artificial intelligence driven tool for accurate mandibular canal segmentation on CBCT. Journal of Dentistry. 2022;116:103891.

47. Lim H-K, Jung S-K, Kim S-H, Cho Y, Song I-S. Deep semi-supervised learning for automatic segmentation of inferior alveolar nerve using a convolutional neural network. BMC Oral Health. 2021;21:1-9.

48. Ariji Y, Mori M, Fukuda M, Katsumata A, Ariji E. Automatic visualization of the mandibular canal in relation to an impacted mandibular third molar on panoramic radiographs using deep learning segmentation and transfer learning techniques. Oral Surgery Oral Medicine Oral Pathology and Oral Radiology. 2022.

49. Orhan K, Bilgir E, Bayrakdar IS, Ezhov M, Gusarev M, Shumilov E.

Evaluation of artificial intelligence for detecting impacted third molars on cone-beam computed tomography scans. Journal of Stomatology, Oral and Maxillofacial Surgery. 2021;122:333-7.

50. Celik ME. Deep Learning Based Detection Tool for Impacted Mandibular Third Molar Teeth. Diagnostics. 2022;12:942.

51. Yoo J-H, Yeom H-G, Shin W, Yun JP, Lee JH, Jeong SH, et al. Deep learning based prediction of extraction difficulty for mandibular third molars. Scientific Reports. 2021;11:1-9.

52. Fukuda M, Ariji Y, Kise Y, Nozawa M, Kuwada C, Funakoshi T, et al. Comparison of 3 deep learning neural networks for classifying the relationship between the mandibular third molar and the mandibular canal on panoramic radiographs. Oral Surgery Oral Medicine Oral Pathology and Oral Radiology. 2020;130:336-43.

국문초록

딥러닝을 이용한 하악 제3대구치와 하악관의 3차원 위치 관계를 위한 자동 분류 프레임워크

연구 배경: 하악 제3대구치 발치 중 하치조 신경 손상에 대한 적절한 위험 평가 및 치료 계획을 위해서는 하악관과의 상대적인 협측 또는 설측 관계를 확인하는 것이 특히 중요하다. 그러나 경험이 부족한 임상의 및 초보자의 경우 가변적인 밀도 값과 노이즈로 인해 CBCT 영상에서 하악관의 위치와 경로를 식별하기 어렵다. 또한 CBCT 이미지의 각 조각에서 수동 분할은 시간이 많이 걸리고 노동 집약적인 작업이다. 이러한 이유로 본 연구는 CBCT 영상에서 제3대구치와 하악관을 자동으로 분할하고 이 두 구조 간의 위치 관계를 분류할 수 있는 CAD(Computer-Aided Diagnosis) 프레임워크를 개발하기 위해 수행되었다.

연구 방법: 본 연구는 CBCT 데이터 세트를 훈련 세트(24명의 환자), 검증 세트(8명의 환자) 및 테스트 세트(18명의 환자)로 나누어 진행되었다. CBCT의 2D 축 슬라이스에서 제3대구치와 하악관 모두의 분할을 예측하기 위해 인코더-디코더 네트워크를 훈련하였다. 그런 다음 공간 및 기하학 정보를 학습하여 제3대구치와 하악관 사이의 상대적 협측-언어 관계를 분류하기 위해 다중 볼륨 입력이 있는 기하학 유도 3D 분류 네트워크(GCNN)를 훈련하였다. 이후, 제안된 방법을

통해 예측된 하악 제3대구치와 하악관의 형상의 정확도와 이들 사이의 위치 관계 예측 정확도를 평가하여 합리적인 CAD 시스템인지 평가하였다.

연구 결과: 자동 분할에서 Dense U-Net은 제3대구치 분할의 경우 DSC 값 0.920±0.131, 하악관 분할의 경우 DSC 값 0.861±0.096을 달성하였다. 제3대구치와 하악관 사이의 협설 관계의 자동 분류에서 GCNN은 1.00의 정확도를 달성하였다.

결 론: 본 연구에서는 CBCT 영상에서 제3대구치와 하악관의 자동 분할을 수행하고 딥 러닝을 사용하여 이 두 구조 간의 위치 관계를 분류하는 2단계 CAD 프레임워크를 개발하였다.

주요어: 딥러닝, 합성곱 신경망, 자동 분할, 자동 분류, 컴퓨터 지원 진단 (CAD), 제3대구치 발치 수술

학 번: 2020-27763